Article

Assessing Soil Physical Quality in a Layered Agricultural Soil: A Comprehensive Approach Using Infiltration Experiments and Time-Lapse Ground-Penetrating Radar Surveys

Simone Di Prima [1,*], Gersende Fernandes [2,3], Maria Burguet [4], Ludmila Ribeiro Roder [5,6], Vittoria Giannini [7], Filippo Giadrossich [3], Laurent Lassabatere [2] and Alessandro Comegna [1]

1   Department of Agricultural, Forestry, Food and Environmental Sciences (DAFE), University of Basilicata, 85100 Potenza, Italy; alessandro.comegna@unibas.it
2   Univ Lyon, Université Claude Bernard Lyon 1, CNRS, ENTPE, UMR 5023 LEHNA, 69518 Vaulx-en-Velin, France; gersende.fernandes@entpe.fr (G.F.); laurent.lassabatere@entpe.fr (L.L.)
3   Department of Agricultural Sciences, University of Sassari, Viale Italia, 39A, 07100 Sassari, Italy; fgiadrossich@uniss.it
4   Dipartimento per l'Innovazione Umanistica, Scientifica e Sociale (DIUSS), University of Basilicata, 85100 Potenza, Italy; maria.burguet@unibas.it
5   Architecture, Design and Urban Planning, University of Sassari, Piazza Duomo, 6, 07041 Alghero (Sassari), Italy; l.ribeiroroder@studenti.uniss.it
6   School of Agriculture, São Paulo State University (UNESP), Fazenda Experimental Lageado, Botucatu 18610-034, SP, Brazil
7   Department of Agronomy, Food, Natural Resources, Animals and Environment—DAFNAE, University of Padua, Agripolis Campus, Viale dell'Università 16, 35020 Legnaro (Padova), Italy; vittoria.giannini@unipd.it
*   Correspondence: simone.diprima@unibas.it

Abstract: Time-lapse ground-penetrating radar (GPR) surveys, combined with automated infiltration experiments, provide a non-invasive approach for investigating the distribution of infiltrated water within the soil medium and creating three-dimensional images of the wetting bulb. This study developed and validated an experimental protocol aimed at quantifying and visualizing water distribution fluxes in layered soils under both unsaturated and saturated conditions. The 3D images of the wetting bulb significantly enhanced the interpretation of infiltration data, enabling a detailed analysis of water movement through the layered system. We used the infiltrometer data and the Beerkan Estimation of Soil Transfer parameters (BEST) method to determine soil capacitive indicators and evaluate the physical quality of the upper soil layer. The field survey involved conducting time-lapse GPR surveys alongside infiltration experiments between GPR repetitions. These experiments included both tension and ponding tests, designed to sequentially activate the soil matrix and the full pore network. The results showed that the soil under study exhibited significant soil aeration and macroporosity (represented by AC and p_{MAC}), while indicators related to microporosity (such as $PAWC$ and RFC) were notably low. The RFC value of 0.55 m^3 m^{-3} indicated the soil's limited capacity to retain water relative to its total pore volume. The $PAWC$ value of 0.10 m^3 m^{-3} indicated a scarcity of micropores ranging from 0.2 to 30 μm in diameter, which typically hold water accessible to plant roots within the total porosity. The saturated soil hydraulic conductivity, K_s, values ranged from 192.2 to 1031.0 mm h^{-1}, with a mean of 424.4 mm h^{-1}, which was 7.9 times higher than the corresponding unsaturated hydraulic conductivity measured at a pressure head of h = −30 mm (K_{-30}). The results indicated that the upper soil layer supports root proliferation and effectively drains excess water to the underlying limestone layer. However, this layer has limited capacity to store and supply water to plant roots and acts as a restrictive barrier, promoting non-uniform downward water movement, as revealed by the 3D GPR images. The observed difference in hydraulic conductivity between the two layers suggests that surface ponding and overland flow are generated through a saturation excess mechanism. Water percolating through the soil can accumulate above the limestone layer, creating a shallow perched water table. During extreme rainfall events, this water table may rise, leading to the complete saturation of the soil profile.

1. Introduction

Soil is the basis of agriculture and its management has significant impacts on its biochemical, ecological, and physical functions [1]. To evaluate these impacts, the notion of soil quality was developed. Doran and Parkin [2] suggested assessing soil quality as "the capacity of a soil to function within ecosystem boundaries to sustain biological productivity, maintain environmental quality, and promote plant and animal health," including human health. Even if that notion has been criticized, it puts forward the complexity and multi-functionality of soils [3]. Good soil quality is needed to keep agriculture sustainable and resilient over time. Thus, the choice of parameters to study and the methods used for soil quality assessment are important. This paper focuses specifically on the soil physical quality (SPQ), which is linked to chemical, biological, and ecological aspects.

To evaluate SPQ, several physical indicators associated with soil water cycle functions—such as air capacity, plant-available water capacity, relative field capacity, soil microporosity, and saturated hydraulic conductivity—are well documented and frequently used in the literature [3–5]. These parameters can be derived from soil water retention and hydraulic conductivity curves, which accurately represent the characteristics of the soil under study. These curves can be generated using the BEST method. This method involves conducting a field infiltration test with a predetermined water volume and collecting soil samples to determine bulk density, initial water content, and particle size distribution in the laboratory [6].

However, the pore network characterization shows greater significance in the SPQ assessment than the study of parameters derived from disturbed aggregates [7]. The soil structure, and, in particular, the soil macroporosity, can be determined in different ways, most of which are time-consuming, partial, and destructive. Dyes and tracers are, for example, injected into soils before excavation, to visualize the preferential flow paths [8]. To improve the determination of the pore network, geophysical tools like Ground Penetrating Radar (GPR) are valuable as they are faster, more precise, non-invasive, and sensitive to water [9]. GPR is a system composed of two antennas, one emitting and the other receiving pulses of electromagnetic waves. When the material or region reached by the wave in the soil has a change in its dielectric properties compared to the surrounding environment, a part of the wave is reflected and subsequently detected by the second antenna. A change in the received signal appears. As the water has a strong difference in dielectric properties compared with the (dry) soil, GPR has great potential for visualizing and monitoring water in the soil. Indeed, [10] observed drainage and storage dynamics with GPR, before and after rain events, while [11] used GPR to study hydrological dynamics at the hillslope scale. Time-lapse GPR surveys are also conducted to image subsurface responses to irrigation [12].

Recently, the integration of an infiltration experiment with a GPR survey was conducted to enhance the understanding of preferential flow in urban areas [13]. This former study focused on the GPR part but shows that GPR and infiltrometers are possibly coupled. Thus, both infiltrometers and GPR devices can be utilized to characterize intrinsic soil parameters and the pore network, facilitating the assessment of SPQ.

However, this experiment does not allow for differentiating the flows from the matrix and the macropores. To do so, different infiltrometer devices such as disc and ring infiltrometers can be used [14], the first allowing a tension experiment that only activates the matrix (smaller pores), and the second activating all the pores (macropores included) with a pond experiment. With the first device, for example, Watson and Luxmoore [15] determined the concentration of different sizes of pores at the soil surface. The second device, the ring infiltrometer, is used in many ways in the literature, especially to determine the basic infiltration parameters, e.g., [16–20].

In this study, we integrated GPR surveys with two automated infiltration experiments at the Ottava experimental station (University of Sassari, Sassari, Italy) to evaluate SPQ,

e.g., [13,21–23]. The objective was to enhance understanding of the soil pore network and assess several key indicators: (i) air capacity (AC m^3 m^{-3}), (ii) plant-available water capacity ($PAWC$ m^3 m^{-3}), (iii) relative field capacity (RFC–), and (iv) soil macroporosity (p_{MAC} m^3 m^{-3}). The site was selected for its distinctive soil composition consisting of two layers (sandy clay loam and limestone). The study aimed to assess the efficacy of GPR and infiltrometers in determining SPQ indicators, delineating water movement across both soil layers, and elucidating infiltration mechanisms. Distinctions were drawn between experiments that selectively engaged the soil matrix (tension experiment) and those that encompassed the entire pore network (single-ring experiment). Many previous studies have compared tension and ponding infiltration measurements, e.g., [24,25], and more recently, GPR has been used to enhance the interpretation of water dynamics during the infiltration process, e.g., [13,21–23]. However, to our knowledge, this is the first time a protocol integrating all these methodologies has been presented.

2. Materials and Methods

2.1. Experimental Site

At the Ottava experimental station (located at 40°46′47″ N, 8°29′45″ E), affiliated with the University of Sassari (Sardinia, Italy), an experimental trial was initiated in October 2019. The trial involved intercropping *Cynara cardunculus* cv Bianco Avorio with various cover crops, including *Vicia villosa* Roth, *Camelina sativa* (L.) Crantz, *Eruca sativa* L. and spontaneous vegetation. For the present experiment, in May 2020, the field measurements were carried out on a 20 m^2 sampling plot where *Cynara cardunculus* was intercropped with spontaneous vegetation.

The climate is typically Mediterranean, while the long-term (1981–2019) average annual rainfall is around 510 mm. As per USDA guidelines, the upper soil horizon was characterized as sandy clay loam (Table 1), with a thickness of 0.3 m. Beneath this layer, there exists a limestone stratum serving as a restrictive layer (typic Xerochrepts).

Table 1. Coordinates and percentage of clay, silt, and sand content using USDA soil classification systems for depth ranging from 0 to 0.2 m. It also includes soil textural classification, soil organic carbon (OC) content, dry soil bulk density (ρ_b), initial volumetric soil water content (θ_0), final volumetric water content at the end of the TI test, $\theta_{TI(h=-30)}$ (corresponding to $h = -30$ mm), saturated volumetric water content (θ_s), and soil porosity (ε) for the soils sampled at the Ottava site. Standard deviations are provided in parentheses.

Variables	
Coordinates	40°46′46.82″ N
	8°29′45.89″ E
Clay [%]	24.8 (2.67)
Silt [%]	22.6 (4.92)
Sand [%]	52.6 (3.15)
Textural classification	sandy clay loam
OC [g kg^{-1}]	15.7 (0.92)
ρ_b [g cm^{-3}] (0–0.1 m depth).	1.298 (0.09)
ρ_b [g cm^{-3}] (0.1–0.2 m depth).	1.462 (0.07)
θ_0 [m^3 m^{-3}]	0.072 (0.01)
$\theta_{TI(h=-30)}$ [m^3 m^{-3}]	0.348 (0.01)
θ_s [m^3 m^{-3}]	0.405 (0.02)
ε [m^3 m^{-3}] (0–0.1 m depth).	0.501 (0.03)
ε [m^3 m^{-3}] (0.1–0.2 m depth).	0.445 (0.03)

2.2. Time-Lapse Ground-Penetrating Radar Survey

The ground-penetrating radar (GPR) survey was employed to enhance the interpretation of infiltration data and to highlight distinct hydraulic responses between the surface soil and the underlying limestone layer. The GPR survey utilized an IDS (Ingegneria Dei

Sistemi S.p.A., Pisa, Italy) Ris Hi Mod v. 1.0 system equipped with a 900 MHz antenna mounted on a GPR cart. A GPR grid (1 m × 1 m) was established using white/red signaling tape, comprising twelve transects (six vertical and six horizontal) spaced 0.2 m apart.

The experimental protocol consisted of six stages (Figure 1): (i) collection of the initial 12 radargrams across the entire grid under dry soil conditions prior to infiltration tests; (ii) conducting a tension infiltration test at the grid center, during which the grid was removed to activate only the soil matrix; (iii) performing a second GPR scan of the grid to observe differences compared to the initial scans, influenced by water infiltration into the matrix flow region; (iv) implementing a single-ring infiltration test using a solution of brilliant blue dye (E133) on the same surface as the tension test to infiltrate water through the entire pore network; (v) conducting a final GPR scan of the grid to illustrate differences from the initial survey scans due to water infiltration affecting both the matrix and larger pores; and (vi) excavating the soil profile to directly observe wetted conditions. In total, 36 radargrams (3 grid scans × 12 transects) were collected using the time acquisition mode, with the GPR cart, moving along each transect and marking positions every 0.2 m at intersections.
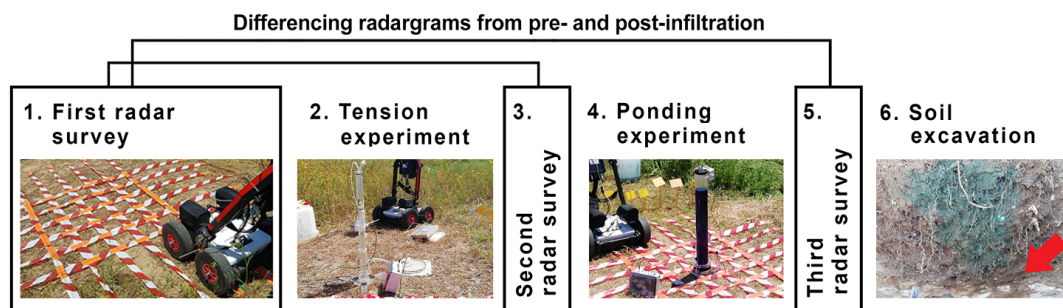

Figure 1. Flowchart outlining the process to generate a 3D image of the wetting bulb. The arrow indicates the funneling flow path through the limestone layer.

2.3. Infiltration Experiments for Assessing Soil Physical Quality of Agricultural Soil

We integrated infiltration data with the Beerkan Estimation Soil Transfer (BEST) method [6] to assess SPQ indicators. These indicators represent soil parameters that quantify the extent or quality of soil physical characteristics [26]. In agricultural contexts, these indicators gauge the soil's capacity to retain and supply water and air, essential for crop growth [27].

We conducted ten single-ring infiltration tests at randomly selected locations within a 5 × 4 m sampling plot, employing the automated single-ring infiltrometers described by Concialdi et al. [28]. For each experiment, a stainless steel ring with a 15 cm inner diameter was inserted 1 cm into the ground, followed by the application of varying volumes of water (ranging from 270 to 280 mm), over an area of 176.7 cm^2 [6]. For detailed procedures on infiltrometer application, please consult Di Prima [18] and Di Prima et al. [29]. Additionally, the software code for processing raw infiltrometer data is available at bestsoilhydro.net (accessed on 8 October 2024), and the treatment protocol can be accessed online [30].

To estimate soil hydraulic parameters for the van Genuchten [31] water retention curve $\theta(h)$, we utilized the BEST-steady algorithm developed by Bagarello et al. [32], incorporating the Burdine [33] condition:

$$\theta(h) = \theta_s \left[1 + (\alpha|h|)^n \right]^{-m} \tag{1a}$$

$$m = 1 - \frac{2}{n} \tag{1b}$$

where h (mm) is the water pressure head, α (mm^{-1}) is the van Genuchten pressure scale parameter, and θ_s (m^3 m^{-3}) is the saturated soil water content.

Upon completion of the infiltration tests, saturated soil samples were collected to ascertain the gravimetric water content. These measurements were subsequently utilized

to calculate the saturated volumetric water content θ_s from the bulk density. The shape parameter n was derived from the particle size distribution (PSD) using the pedotransfer functions provided in the BEST method. Soil sorptivity S (mm h$^{-0.5}$) and saturated hydraulic conductivity K_s (mm h^{-1}) were estimated using the following equations [29]:

$$S = \sqrt{\frac{i_s}{A + \frac{C}{b_s}}} \tag{2}$$

$$K_s = \frac{C\, i_s}{A\, b_s + C} \tag{3}$$

where i_s (mm h^{-1}) and b_s (mm) are, respectively, the slope and the intercept of the linear portion of the cumulative infiltration versus time plot. These are used to determine the constants A (mm^{-1}) and C, which are defined as follows [34,35]:

$$A = \frac{\gamma}{r(\theta_s - \theta_0)} \tag{4a}$$

$$C = \frac{1}{2(1-\beta)} ln\left(\frac{1}{\beta}\right) \tag{4b}$$

where θ_0 (m^3 m^{-3}) represents the initial volumetric water content of the soil, r (mm) denotes the radius of the infiltration source, and γ and β are infiltration coefficients, typically set at $\gamma = 0.75$ and $\beta = 0.6$ [35].

Finally, following the methodology of Lassabatere et al. [6], the structure-dependent scale parameter (α) was derived from the textural parameter (n) and infiltrometer data (S and K_s). For further details on the BEST procedure, refer to Angulo-Jaramillo et al. [36].

We also conducted three tension infiltration (TI) tests within the same sampling plot at randomly selected locations. We applied a suction of 30 mm using a SW-080B infiltrometer with a 0.24 m diameter porous plate. At the end of the experiments, we sampled the wet soil to determine the gravimetric water content. Then, these measurements were used to determine the final volumetric water content from the bulk density corresponding to $h = -30$ mm, $\theta_{TI(h=-30)}$ (m^3 m^{-3}). According to Angulo-Jaramillo et al. [37], the soil hydraulic conductivity at the imposed suction, K_{-30} (mm h^{-1}), was calculated as follows:

$$K_{-30} = \frac{3}{2-\beta}\left[C_2 - \frac{\gamma C_1^2}{r\left(\theta_{TI(h=-30)} - \theta_0\right)}\right] \tag{5}$$

where c_1 (mm h$^{-0.5}$) and c_2 (mm h^{-1}) are infiltration coefficients [35], which were determined to fit the two-term infiltration model by Philip [38] to the experimental data. The fitting procedure was carried out using the method referred to as cumulative infiltration CI, e.g., [39].

In addition to the previous infiltration measurements, one test of each type (TI and Beerkan) was conducted at the center of the GPR survey grid (Figure 1). While the tension tests were aimed at activating the soil matrix alone, the Beerkan tests were aimed at activating the whole pore network. These two tests were designed to explain the following: (i) the amplitude variations between repeated GPR radargrams from the initial and second surveys, attributed to water infiltration within the matrix flow region (tension test), and (ii) the amplitude variations between the initial and third surveys, resulting from water movement throughout the entire pore network, including macropores formed by biotic activity (grass roots and earthworms) (single-ring test). The tension test utilized tap water, whereas the Beerkan test involved infiltrating a solution containing 1 g L^{-1} of brilliant blue dye (E133). Employing these two fluids in tandem enabled us to distinguish differences between water and dye distribution patterns during the soil excavation conducted following the third GPR survey (Figure 1).

Six undisturbed soil cores were extracted from the sampling plot at depths of 0–0.3 m. Three samples were collected at 0–1 m and three others at 0.1–0.2 m. These samples were utilized to ascertain the dry soil bulk density, ρ_b (g cm^{-3}), and soil porosity, ε (m^3 m^{-3}). Additionally, five disturbed soil samples were collected from depths of 0 to 0.2 m to determine the particle size distribution (PSD). This was achieved using conventional methodologies, involving a H_2O_2 pretreatment to remove organic matter and clay deflocculation with sodium metaphosphate and mechanical agitation [40]. Specifically, the fine fractions were quantified via the hydrometer method, while the coarse fractions were determined through mechanical dry sieving. According to USDA standards, three particle size fractions were identified: clay (0–2 μm), silt (2–50 μm), and sand (50–2000 μm).

The site was characterized by averaged values of ρ_d, θ_0, $\theta_{TI(h=-30)}$, θ_s, ε, n, m, K_{-30}, K_s and α. The hypothesis of normality of the non-transformed and log-transformed parameter distributions was checked by the Kolmogorov–Smirnov test. Parameter means were determined based on the statistical distribution of the data, employing arithmetic means for normally distributed data and geometric means for log-normally distributed data. To quantify the associated variability, the coefficient of variation (CV) was calculated for arithmetic means, while the geometric coefficient of variation (GCV) was calculated for geometric means [41].

We employed the BEST averaged parameters to derive several key parameters from the soil water retention curve (Equation (1)): the permanent wilting point soil water content (θ_{PWP} m^3 m^{-3}) at $h = -150$ m, the field capacity soil water content (θ_{FC}, m^3 m^{-3}) at $h = -1$ m, and the saturated volumetric water content of the soil matrix (θ_m, m^3 m^{-3}) at $h = -0.1$ m. These parameters, in conjunction with θ_s, were utilized to estimate the following capacitive SPQ indicators: air capacity (*AC*, m^3 m^{-3}), plant-available water capacity (*PAWC*, m^3 m^{-3}), relative field capacity (*RFC*, –), and soil macroporosity (p_{MAC}, m^3 m^{-3}) (Table 2). The indicators considered in this study, along with the associated optimal ranges or critical limits, were selected based on the study by Reynolds et al. [42].

Table 2. Estimated values of the selected soil physical quality (SPQ) indicators along with their corresponding optimal ranges or critical thresholds for the sampled soils at the Ottava site.

Soil Physical Quality Indicator	Description	Ranges or Critical Limits	Evaluation Class
Soil organic carbon content, *OC* [g kg^{-1}]	Strong indirect effects on soil physical quality	$30 \leq OC \leq 50$	optimal
		$23 \leq OC < 30$ and $50 < OC \leq 60$	intermediate
		$OC < 23$ and $OC > 60$	poor
Structure stability index, *SSI* [%] = 1.724 OC%/(silt% + clay%) × 100		$SSI > 9$	stable structure
		$7 < SSI \leq 9$	low risk of structural degradation
		$5 < SSI \leq 7$	high risk of degradation
		$SSI \leq 5$	structurally degraded soil
Air capacity, *AC* [m^3 m^{-3}] = $\theta_s - \theta_{FC}$	Root zone aeration	≥ 0.14	good
		$0.10 \leq AC < 0.14$	intermediate
		<0.10	poor
where θ_{FC} [m^3 m^{-3}] is the field capacity (gravity drained) soil water content, corresponding to $h = -1$ m.			
Plant-available water capacity, *PAWC* [m^3 m^{-3}] = $\theta_{FC} - \theta_{PWP}$	Soil's ability to store and provide water available to plant roots	≥ 0.20	ideal
		$0.15 \leq PAWC < 0.20$	good
		$0.10 \leq PAWC < 0.15$	limited
		<0.10	poor
where θ_{PWP} [m^3 m^{-3}] is the permanent wilting point soil water content, corresponding to $h = -150$ m.			
Relative field capacity, *RFC* [−] = θ_{FC}/θ_s	Soil's ability to store water and air relative to the soil's total pore volume	$0.6 \leq RFC \leq 0.7$	optimal
		<0.6	limited (water limited soil)
		>0.7	limited (aeration limited soil)

Table 2. *Cont.*

Soil Physical Quality Indicator	Description	Ranges or Critical Limits	Evaluation Class
Macroporosity, p_{MAC} [m^3 m^{-3}] = $\theta_s - \theta_m$	Soil's ability to quickly drain excess water and facilitate root proliferation	≥ 0.07	optimal
		$0.04 \leq p_{MAC} < 0.07$	intermediate
		< 0.04	poor

where θ_m [m^3 m^{-3}] is the saturated volumetric water content of the soil matrix, corresponding to $h = -0.1$ m.

2.4. GPR Data Processing and Solid Modeling

A Ground-Penetrating Radar (GPR) output typically comprises a radargram, which consists of time-series reflections that provide cross-sectional profiles of subsurface depth over time [43]. The collected radargrams were processed using Reflexw software version 4.0 (Sandmeier Scientific Software, Karlsruhe, Germany). The processing protocol included the following: (i) trace interpolation to ensure equidistant spacing between markers at survey line intersections, with an increment of 0.2 m, (ii) static time shift adjustment to synchronize the arrival of direct ground waves to 0 ns, (iii) bandpass filtering within the temporal domain, (iv) application of an exponential gain function to counteract GPR signal attenuation with depth; as per Truss et al. [10], the same gain curve, established from pre-wetting data, was uniformly applied across all time-lapse data, (v) implementation of a background removal filter to mitigate horizontal noise, and (vi) compression in both temporal and spatial dimensions to minimize computational time required for subsequent processing steps, such as 3D interpolation.

Amplitude values, G, from all radargrams within the grid were aggregated to form a comprehensive XYZG dataset, where X, Y, and Z denote spatial coordinates (easting, northing, and elevation). Elevation, Z, was derived from wave travel time recorded during GPR acquisition, with an assumed wave velocity of 0.11 m ns^{-1}, as determined from the detection of subsurface objects at known depths. Consequently, both pre- and post-wetting XYZG datasets were obtained. Subsequently, additional datasets were created based on the absolute differences between pre- and post-wetting G values. The movement of water within the unsaturated zone induced variations in the dielectric contrast between layers, thereby altering the reflection coefficient [10]. These alterations were manifested as changes in amplitude. Therefore, the differenced datasets were constructed to emphasize amplitude fluctuations between repeated GPR radargrams acquired along the same survey lines before and after the infiltration test, e.g., [23,44]. It was hypothesized that the absolute difference between pre- and post-wetting amplitude values was inversely correlated with the soil water pressure head [45]. Consequently, the most significant reflection differences were anticipated at the location of the saturated soil bulb extending outward from the infiltration surface, with decreasing reflection differences in the partially saturated zone surrounding the wetting bulb. In this zone, the water pressure head diminishes as the wetting front advances due to soil capillarity from the saturated bulb [37].

The RockWorks 17 software [46] was employed in conjunction with the inverse-distance anisotropic modeling technique to execute a 3D interpolation of the differenced GPR datasets. This anisotropic search methodology enhances the interpolation accuracy of voxel (volumetric picture element) values located between clusters of data points and has been effectively utilized in numerous geophysical studies, e.g., [47–49]. The interpolation algorithm assigned values to voxel based on a weighted average of adjacent data points within each 90-degree sector around the node. The weighting of each data point's amplitude value was inversely proportional to the square of its distance from the voxel node (inverse-distance squared).

3. Results and Discussion

3.1. Detection of Wetting Zones through GPR Data

The GPR-based delineation of the wetting bulb at the Ottava site is presented. The 3D renderings (Figure 2a,e) distinctly outlined the dimensions and configurations of the

wetting bulb generated during both the tension and Beerkan infiltration tests conducted on the identical surface area. Initially, the infiltration bulbs were identified through a comprehensive 360-degree examination of the 3D renderings. Subsequently, horizontal and vertical cross-sections were extracted from the 3D models to pinpoint regions with significant reflection differences, indicative of wetted soil patches beneath the primary wetting front (Figure 2: TI test in subpanels b–d and Beerkan test in subpanels f–h). These cross-sections were then compared with the direct observations of the infiltration bulb, exposed by sectioning the soil along a vertical plane at the conclusion of the third GPR survey (Figure 1). The congruence between the observed shapes provided a robust indication of the accuracy of the 3D interpolation procedure in mapping the wetted patterns. This finding corroborated the experimental results of a prior study by Di Prima et al. [13].
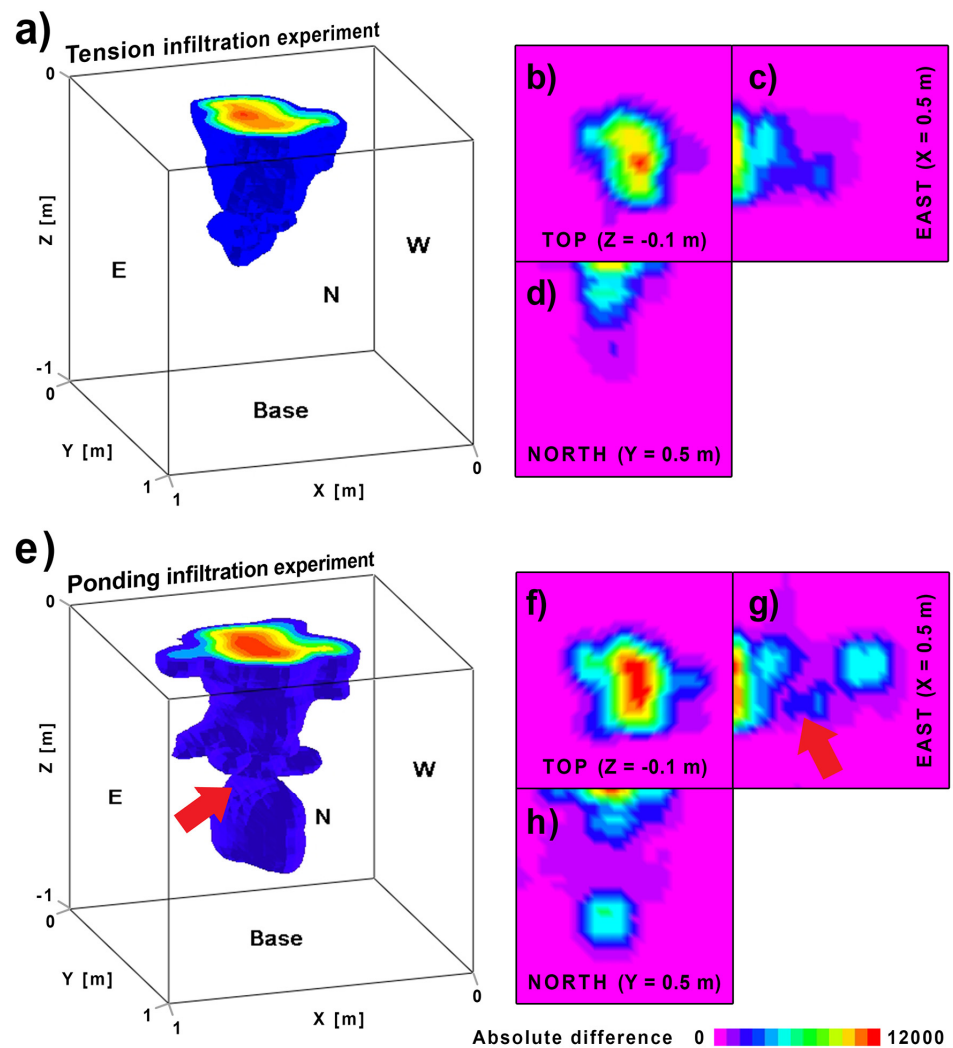

Figure 2. Three-dimensional representations of the wetting zones obtained from ground-penetrating radar surveys conducted before and after wetting, during (**a**) tension and (**e**) ponding infiltrometer experiments at the Ottava site. Panels (**b,f**) illustrate horizontal cross-sections taken from the 3D models at a depth of −0.1m from the soil surface. Panels (**c,g**) present vertical cross-sections oriented north–south with a view to the east, while panels (**d,h**) show vertical cross-sections oriented west–east within a view to the north. The red arrows highlight the detected flow channeling through the limestone layer (see Figure 1 for reference).

During the tension infiltration (TI) test, an applied suction of 30 mm (equivalent to a water pressure head of −30 mm) restricted water flow to the soil matrix, thereby excluding pores with radii > 0.5 mm from the infiltration process [45]. The comparison of radargrams

from the initial and subsequent GPR surveys enabled us to discern amplitude variations attributable to water movement within the matrix flow region. As anticipated for capillary-driven infiltration, the resulting wetting bulb exhibited a regular, quasi-hemispherical configuration with a uniform water distribution (Figure 2a,b), primarily extending through the upper soil horizon to an approximate depth of 0.3 m (Figure 2c,d).

The differentiation between the repeated radargrams of the first and third GPR surveys allowed us to highlight the amplitude fluctuations as a result of the water infiltrating throughout the entire pore system More specifically, in this case, the wetting bulb is the result of the water infiltrated during both the TI and Beerkan tests, which were carried out on the same infiltration surface. During the ponding test, given that the smaller pores were already filled, the water movement occurred mainly into the larger pores (>0.5 mm), determining a smaller wetting pattern in comparison to that generated during the TI test, which highlighted the occurrence of a mainly vertical gravity-driven movement through the topsoil [50], as shown from the dye pattern in Figure 1 (Step 6: Soil excavation). In the subsequent phase, as the advancing wetting front reached the underlying limestone stratum at a depth of 0.3 m, the infiltration rates observed at the soil surface diminished owing to the reduced hydraulic conductivity of the stratum. The three-dimensional representation facilitated the identification of flow channeling through the limestone layer (Figure 2g), corroborated by observations in Figure 1.

In this scenario, the wetted region exhibited an extended and uneven form (Figure 2g,h), aligning with the interface of the limestone layer (red arrows in Figure 1 Step 6, Figure 2e,g). Both the 3D diagram and the patterns from dye staining indicated that water infiltrated through this impermeable layer via a funneling mechanism. Specifically, the limestone layer, characterized by low hydraulic conductivity, acted as a capillary barrier that directed flow into a relatively confined path, a common phenomenon known as funneled flow [46]. Consequently, flow channeling was observed at the layer interfaces, specifically at a depth of 0.3 m.

3.2. Water Infiltration and Application of the BEST Algorithm

Evidence of the flow dynamics described above, and observed from the 3D diagrams, was also found when analyzing infiltration data. Indeed, all Beerkan infiltration curves showed a sudden decrease in infiltration rate when the wetting front encountered the limestone layer. Lassabatere et al. [51] suggest that water infiltration data should be considered indicative of the hydraulic characteristics of the most impermeable layer. Therefore, characterizing the hydraulic properties of the topsoil required us to discriminate the infiltration process into two different stages: a first stage when water infiltrated only into the surface layer, and a subsequent phase when the wetting front reached the interface between layers. The decline in infiltration rate was not readily discernible from visual examination of the cumulative infiltration curve (Figure 3a) but became apparent upon applying the cumulative linearization method CL, [52] (Figure 3b). More specifically, all the linearized curves showed a convex shape, which is expected in the case of layered soils with an underlying less permeable layer [25]. Conversely, for ideal situations, namely for uniformly unsaturated, rigid, and homogeneous soils, linearized infiltration data are expected to show an increasing trend that is characterized by a practically unique slope [37].

Thus, we characterized all the linearized Beerkan plots ($I\sqrt{t}$ vs. $\sqrt{t}$) by an initial ascending linear segment, followed, after a knee point, by a more or less distinct reduction in slope. Subsequently, we computed the slope and intercept values for both the early and later phases of the infiltration processes.

As shown in Figure 3b, for the case of a single Beerkan test, we also calculated the abscissa ($\sqrt{t}$) of the intersection point of the two straight lines. This threshold split the infiltration data into two subsets representative of the two stages occurring when water moved across the layering profile: a first stage (first linear portion) when water infiltrated into the upper layer, and a second stage (second liner part) when water started to infiltrate into the underlying limestone layer. The infiltration data corresponding to the first stage

were subsequently used for assessing the soil physical quality of the upper soil layer (Figure 3c).
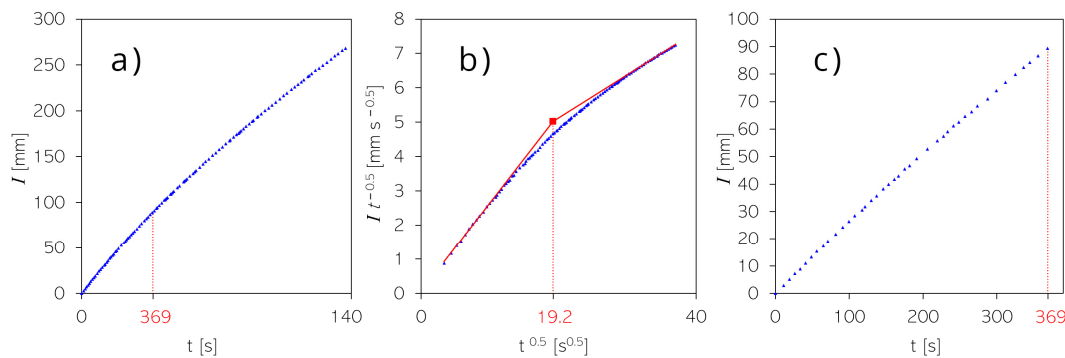

Figure 3. Example of the procedure adopted for detecting flow impedance owing to the hydraulic resistance exerted by the underlying limestone layer. (**a**): Entire cumulative infiltration curve [$I(t)$ vs. t]. (**b**): Data linearized according to the cumulative linearization (CL, Smiles and Knight, 1976) method ($I\sqrt{t}$ vs. $\sqrt{t}$). The abscissa ($\sqrt{t}$) of the intersection point of the two straight lines splits the infiltration data into two subsets. (**c**): Cumulative infiltration data representative of the first stage when water infiltrates into the upper layer.

The BEST-steady algorithm was employed to derive parameters n, m, α and K_s from textural and infiltrometer data (Table 3). Statistical analysis using the Kolmogorov–Smirnov test indicated that K_s data followed a log-normal distribution. Consequently, the geometric mean and the geometric coefficient of variation were computed for K_s [41]. Conversely, all other parameters exhibited normal distributions and were synthesized using the average value and its corresponding variability. K_s values ranged from 192.2 to 1031.0 mm h^{-1}, with a mean of 424.4 mm h^{-1}. Additionally, estimates of K_s were compared with field measurements of unsaturated hydraulic conductivity, K_{-30}, obtained at a pressure head of $h = -30$ mm (K_{-30}). Table 3 summarizes the K_{-30} values measured for the Ottava site. As expected, the hydraulic conductivity increased dramatically in the proximity of the saturation, i.e., for $h = 0$. The K_{-30} values ranged between 33.3 and 70.1 mm h^{-1}. The K_s values estimated by BEST consistently exceeded the measured K_{-30} values, indicating that physically realistic estimates of K_s were obtained across all scenarios, as $K_s > K_{-30}$. Specifically, for the topsoil, BEST provided a mean K_s value that was 7.9 times higher than the corresponding K_{-30}, equivalent to an order of magnitude difference. Such substantial differences between saturated and near-saturated hydraulic conductivity are frequently observed under field conditions, e.g., [53]. These results imply that macropore flow is likely prominent in the topsoil, facilitating rapid drainage of excess water towards the underlying limestone layer. Furthermore, the observed funneling infiltration mechanism through the restrictive limestone layer (Figure 2) and the contrast in hydraulic conductivity between the two layers (Figure 3) imply that ponding on the surface and the generation of overland flow primarily result from a saturation-excess mechanism [54].

Table 3. Sample size (N), minimum (min), maximum (max), mean, and coefficient of variation (CV, %) of the BEST and TI estimations.

Variable	N	Min	Max	Mean	CV
n [−]	5	2.116	2.139	2.127	0.5
m [−]	5	0.055	0.065	0.060	7.6
K_{-30} [mm h^{-1}]	3	33.3	70.1	53.8	34.9
$^{\dagger}K_s$ [mm h^{-1}]	9	192.2	1031.0	424.4	63.8
α [mm^{-1}]	9	0.060	0.244	0.117	54.6

† According to the Kolmogorov-Smirnov test, K_s data were log-normally distributed; thus, the geometric mean and the associated geometric coefficient of variation were calculated for this variable [41]. The arithmetic mean and the associated coefficient of variation were calculated for all other variables.

3.3. Soil Physical Quality Assessment

Two of the six SPQ indicators (*OC* and *SSI*) were directly measured, while the remaining four (capacitive indicators) were derived using the BEST procedure.

The investigated soil had a poor content of organic matter, with a mean *OC* value of 15.7 g kg^{-1}. Also, the low value of the structural stability index (*SSI* = 5.7%) indicates a high risk of soil degradation. These results suggested that the soil was prone to mechanical breakdown of aggregates and the occurrence of sealing phenomena, for instance during intense rainfall events [55]. This hypothesis was corroborated by the observation, during the winter season and in the proximity of the sampled plot, of depositional seal layers. These thin and dense surface layers resulted from the transport of particles physically dispersed by the impacts of raindrops [56]. The particles were carried in suspension by runoff, which may be generated by the above-described mechanism, and finally deposited in correspondence with surface depressions [57].

Figure 4 shows the BEST-deduced water retention curve and the estimated values of the selected capacitive soil physical quality indicators. While the $\theta_{TI(h=-30)}$ and θ_s values were measured from wet soil samples collected, respectively, after the tension and Beerkan infiltration tests, the other parameters (θ_{PWP}, θ_{FC}, and θ_m) were determined from the water retention curve using the mean values of the BEST-deduced shape (*n* and *m*) and scale (*α*) parameters. Almost identical values of the soil water content at the permanent wilting point (θ_{PWP} = 0.12 m^3 m^{-3}) and field capacity (θ_{FC} = 0.22 m^3 m^{-3}) were reported by Giunta et al. [58] for the soil at the Ottava experimental station, thus increasing our confidence in the BEST-deduced parameters. The findings revealed that the soil under study exhibited significant soil aeration and macroporosity (represented by *AC* and p_{MAC}), while indicators related to microporosity (such as *PAWC* and *RFC*) were notably low. A low *RFC* indicates the soil's limited capacity to retain water compared to its total pore volume. *RFC* values below 0.6 may lead to decreased microbial activity due to inadequate soil moisture (water-limited conditions) [27]. A diminished *PAWC* indicates a scarcity of micropores ranging from 0.2 to 30 μm in diameter, which typically hold water accessible to plant roots within the total porosity [4]. Soils with 0.10 ≤ *PAWC* < 0.15 m^3 m^{-3} are frequently categorized as drought-prone [27]. These observations imply that the uppermost soil strata support root growth and efficiently drain surplus water into the underlying limestone layer, yet exhibit restricted capacity to retain and supply water to plant roots.
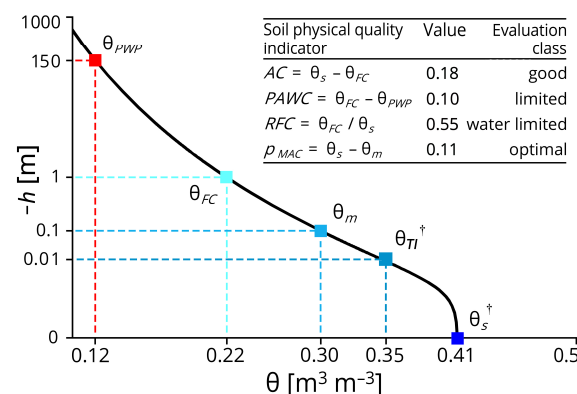

Figure 4. θ_{PWP} [m^3 m^{-3}] is the permanent wilting point soil water content, corresponding to *h* = −150 m. θ_{FC} [m^3 m^{-3}] is the field capacity (gravity drained) soil water content, corresponding to *h* = −1 m. θ_m [m^3 m^{-3}] is the saturated volumetric water content of the soil matrix, corresponding to *h* = −0.1 m. θ_{TI} [m^3 m^{-3}] is the final volumetric water content at the end of the TI test (corresponding to *h* = −0.03 m), θ_s [m^3 m^{-3}] is the saturated volumetric water content. *AC* [m^3 m^{-3}] is the air capacity. *PAWC* [m^3 m^{-3}] is the plant-available water capacity. *RFC* [−] is the relative field capacity. p_{MAC} [m^3 m^{-3}] is the soil macroporosity. † Water content values determined from wet soil samples collected after the tension (θ_{TI}) and Beerkan (θ_s) infiltration tests.

4. Conclusions

In summary, the findings of this study underscore the complex interactions between water dynamics and soil properties in layered systems, leading to the following key conclusions:

- Enhanced Understanding of Water Movement: The 3D images of the wetting bulb significantly improved our understanding of water movement within layered soil, providing valuable insights into the dynamics of water distribution. The images revealed the occurrence of funneling phenomena through the restrictive underlying layer, which acts as a capillary barrier, inhibiting the expansion of the wetting front.
- Hydraulic Conductivity Differences: The observed differences in hydraulic conductivity between the two layers suggest that surface ponding and overland flow are generated through a saturation-excess mechanism. Percolating water can accumulate above the restrictive limestone layer, forming a shallow perched water table that may rise during extreme rainfall events, potentially leading to the complete saturation of the soil profile.
- Soil Physical Quality Indicators: By integrating infiltration data with the BEST method, we determined key soil physical quality indicators in the upper soil layer. The estimated parameters indicated high levels of aeration and macroporosity (AC and p_{MAC}), alongside low values for microporosity indicators ($PAWC$ and RFC). The RFC value of 0.55 m^3 m^{-3} indicated the soil's limited capacity to retain water relative to its total pore volume. The $PAWC$ value of 0.10 m^3 m^{-3} indicated a scarcity of micropores ranging from 0.2 to 30 μm in diameter, which typically hold water accessible to plant roots within the total porosity.
- Implications for Root Proliferation: These findings suggest that the upper soil layer facilitates root proliferation and efficiently drains excess water toward the underlying restrictive layer. However, it has a limited capacity to store and supply water to plant roots.
- Concluding Remarks and Considerations: The use of cover crops or at least inter-alley spontaneous vegetation, recently adopted in the experimental plot, is expected to mitigate, at least in part, these problems over the next years [59]. During periods of intense precipitation, cover crops play a crucial role in mitigating soil erosion and runoff by shielding the soil surface. Simultaneously, they contribute to minimizing nutrient losses by absorbing residual nutrients left in the soil [60]. This dual function underscores their importance in sustainable agricultural practices aimed at enhancing soil health and reducing environmental impacts during extreme weather events. In addition, the presence of cover crop residues may increase the soil organic matter, which also plays a role in producing macrostructures, thereby improving the surface soil structure [42]. Important benefits may also include improved moisture retention because of the mulch provided by cover crop residues [61]. Further studies will be necessary to assess the mitigation role that inter-alley cropping will play during the next agricultural cycles with regard to soil physical quality and the attenuation of the sealing phenomenon.

Author Contributions: S.D.P.: Conceptualization, Methodology, Investigation, Formal analysis, Validation, Visualization, Writing—original draft, Writing—Review and Editing, Funding acquisition. G.F.: Writing—original draft, Writing—Review and Editing. M.B.: Writing—Review and Editing. L.R.R.: Investigation, Data Curation, Writing—Review and Editing. V.G.: Investigation, Writing—Review and Editing. F.G.: Writing—Review and Editing, Funding acquisition. A.C.: Writing—Review and Editing. L.L.: Writing—Review and Editing. All authors have read and agreed to the published version of the manuscript.

Data Availability Statement: The data presented in this study are available on request from the corresponding author.

Conflicts of Interest: The authors declare no conflicts of interest.

References

1. Gomiero, T.; Pimentel, D.; Paoletti, M.G. Environmental Impact of Different Agricultural Management Practices: Conventional vs. Organic Agriculture. *Crit. Rev. Plant Sci.* **2011**, *30*, 95–124. [CrossRef]
2. Doran, J.W.; Parkin, T.B. Defining and Assessing Soil Quality. In *Defining Soil Quality for a Sustainable Environment*; John Wiley & Sons, Ltd.: Hoboken, NJ, USA, 1994; pp. 1–21. ISBN 978-0-89118-930-5.
3. Bünemann, E.K.; Bongiorno, G.; Bai, Z.; Creamer, R.E.; De Deyn, G.; de Goede, R.; Fleskens, L.; Geissen, V.; Kuyper, T.W.; Mäder, P.; et al. Soil Quality—A Critical Review. *Soil Biol. Biochem.* **2018**, *120*, 105–125. [CrossRef]
4. Iovino, M.; Castellini, M.; Bagarello, V.; Giordano, G. Using Static and Dynamic Indicators to Evaluate Soil Physical Quality in a Sicilian Area. *Land Degrad. Develop.* **2016**, *27*, 200–210. [CrossRef]
5. Reynolds, D.; Drury, C.; Tan, C.; Yang, X. Temporal Effects of Food Waste Compost on Soil Physical Quality and Productivity. *Can. J. Soil Sci.* **2015**, *95*, 150511122047004. [CrossRef]
6. Lassabatere, L.; Angulo-Jaramillo, R.; Soria Ugalde, J.M.; Cuenca, R.; Braud, I.; Haverkamp, R. Beerkan Estimation of Soil Transfer Parameters through Infiltration Experiments—BEST. *Soil Sci. Soc. Am. J.* **2006**, *70*, 521. [CrossRef]
7. Rabot, E.; Wiesmeier, M.; Schlüter, S.; Vogel, H.-J. Soil Structure as an Indicator of Soil Functions: A Review. *Geoderma* **2018**, *314*, 122–137. [CrossRef]
8. Allaire, S.E.; Roulier, S.; Cessna, A.J. Quantifying Preferential Flow in Soils: A Review of Different Techniques. *J. Hydrol.* **2009**, *378*, 179–204. [CrossRef]
9. Klenk, P.; Jaumann, S.; Roth, K. Monitoring Infiltration Processes with High-Resolution Surface-Based Ground-Penetrating Radar. *Hydrol. Earth Syst. Sci. Discuss.* **2015**, *12*, 12215–12246. [CrossRef]
10. Truss, S.; Grasmueck, M.; Vega, S.; Viggiano, D.A. Imaging Rainfall Drainage within the Miami Oolitic Limestone Using High-Resolution Time-Lapse Ground-Penetrating Radar. *Water Resour. Res.* **2007**, *43*. [CrossRef]
11. Guo, L.; Chen, J.; Lin, H. Subsurface Lateral Preferential Flow Network Revealed by Time-Lapse Ground-Penetrating Radar in a Hillslope. *Water Resour. Res.* **2014**, *50*, 9127–9147. [CrossRef]
12. Jackisch, C.; Angermann, L.; Allroggen, N.; Sprenger, M.; Blume, T.; Tronicke, J.; Zehe, E. Form and Function in Hillslope Hydrology: In Situ Imaging and Characterization of Flow-Relevant Structures. *Hydrol. Earth Syst. Sci.* **2017**, *21*, 3749–3775. [CrossRef]
13. Di Prima, S.; Winiarski, T.; Angulo-Jaramillo, R.; Stewart, R.D.; Castellini, M.; Abou Najm, M.R.; Ventrella, D.; Pirastru, M.; Giadrossich, F.; Capello, G.; et al. Detecting Infiltrated Water and Preferential Flow Pathways through Time-Lapse Ground-Penetrating Radar Surveys. *Sci. Total Environ.* **2020**, *726*, 138511. [CrossRef] [PubMed]
14. Angulo-Jaramillo, R.; Vandervaere, J.-P.; Roulier, S.; Thony, J.-L.; Gaudet, J.-P.; Vauclin, M. Field Measurement of Soil Surface Hydraulic Properties by Disc and Ring Infiltrometers. A Review and Recent Developments. *Soil Tillage Res.* **2000**, *55*, 1–29. [CrossRef]
15. Watson, K.W.; Luxmoore, R.J. Estimating Macroporosity in a Forest Watershed by Use of a Tension Infiltrometer. *Soil Sci. Soc. Am. J.* **1986**, *50*, 578–582. [CrossRef]
16. Bagarello, V.; Castellini, M.; Di Prima, S.; Iovino, M. Soil Hydraulic Properties Determined by Infiltration Experiments and Different Heights of Water Pouring. *Geoderma* **2014**, *213*, 492–501. [CrossRef]
17. Burgy, R.H.; Luthin, J.N. A Test of the Single- and Double-Ring Types of Infiltrometers. *Eos Trans. Am. Geophys. Union* **1956**, *37*, 189–192. [CrossRef]
18. Di Prima, S. Automated Single Ring Infiltrometer with a Low-Cost Microcontroller Circuit. *Comput. Electron. Agric.* **2015**, *118*, 390–395. [CrossRef]
19. Lassabatere, L.; Di Prima, S.; Angulo-Jaramillo, R.; Keesstra, S.; Salesa, D. Beerkan Multi-Runs for Characterizing Water Infiltration and Spatial Variability of Soil Hydraulic Properties across Scales. *Hydrol. Sci. J.* **2019**, *64*, 165–178. [CrossRef]
20. Nimmo, J.R.; Schmidt, K.M.; Perkins, K.S.; Stock, J.D. Rapid Measurement of Field-Saturated Hydraulic Conductivity for Areal Characterization. *Vadose Zone J.* **2009**, *8*, 142–149. [CrossRef]
21. Di Prima, S.; Fernandes, G.; Marras, E.; Giadrossich, F.; Stewart, R.D.; Abou Najm, M.R.; Winiarski, T.; Mourier, B.; Angulo-Jaramillo, R.; Comegna, A.; et al. Evaluating Subsurface Flow Connectivity in a Pine-Covered Hillslope with Stemflow Infiltration and Ground-Penetrating Radar Surveys. *J. Hydrol.* **2023**, *620*, 129527. [CrossRef]
22. Fan, B.; Liu, X.; Zhu, Q.; Qin, G.; Li, J.; Lin, H.; Guo, L. Exploring the Interplay between Infiltration Dynamics and Critical Zone Structures with Multiscale Geophysical Imaging: A Review. *Geoderma* **2020**, *374*, 114431. [CrossRef]
23. Guo, L.; Lin, H.; Fan, B.; Nyquist, J.; Toran, L.; Mount, G.J. Preferential Flow through Shallow Fractured Bedrock and a 3D Fill-and-Spill Model of Hillslope Subsurface Hydrology. *J. Hydrol.* **2019**, *576*, 430–442. [CrossRef]
24. Lassabatere, L.; Di Prima, S.; Bouarafa, S.; Iovino, M.; Bagarello, V.; Angulo-Jaramillo, R. BEST-2K Method for Characterizing Dual-Permeability Unsaturated Soils with Ponded and Tension Infiltrometers. *Vadose Zone J.* **2019**, *18*, 1–20. [CrossRef]

25. Di Prima, S.; Castellini, M.; Majdi, R.; Abou Najm, M.R.; Stewart, R.D.; Angulo-Jaramillo, R.; Winiarski, T.; Lassabatere, L. Experimental Assessment of a New Comprehensive Model for Single Ring Infiltration Data. *J. Hydrol.* **2019**, *573*, 937–951. [CrossRef]

26. Topp, G.C.; Reynolds, W.D.; Cook, F.J.; Kirby, J.M.; Carter, M.R. Physical Attributes of Soil Quality. Soil Quality for Crop Production and Ecosystem Health. In *Development in Soil Science*; Gregorich, E.G., Carter, M.R., Eds.; Elsevier: New York, NY, USA, 1997; Volume 25, pp. 21–58.

27. Reynolds, W.; Drury, C.; Yang, X.; Fox, C.; Tan, C.; Zhang, T. Land Management Effects on the Near-Surface Physical Quality of a Clay Loam Soil. *Soil Tillage Res.* **2007**, *96*, 316–330. [CrossRef]

28. Concialdi, P.; Di Prima, S.; Bhanderi, H.M.; Stewart, R.D.; Abou Najm, M.R.; Lal Gaur, M.; Angulo-Jaramillo, R.; Lassabatere, L. An Open-Source Instrumentation Package for Intensive Soil Hydraulic Characterization. *J. Hydrol.* **2020**, *582*, 124492. [CrossRef]

29. Di Prima, S.; Lassabatere, L.; Bagarello, V.; Iovino, M.; Angulo-Jaramillo, R. Testing a New Automated Single Ring Infiltrometer for Beerkan Infiltration Experiments. *Geoderma* **2016**, *262*, 20–34. [CrossRef]

30. Automatic Treatment of Raw Data from Automatized Infiltrometer. 2023. Available online: https://youtu.be/nXXxNS3gmCA?si=q6zwfXtiiJb3EXTg (accessed on 8 October 2024).

31. van Genuchten, M.T. A Closed-Form Equation for Predicting the Hydraulic Conductivity of Unsaturated Soils. *Soil Sci. Soc. Am. J.* **1980**, *44*, 892–898. [CrossRef]

32. Bagarello, V.; Di Prima, S.; Iovino, M. Comparing Alternative Algorithms to Analyze the Beerkan Infiltration Experiment. *Soil Sci. Soc. Am. J.* **2014**, *78*, 724. [CrossRef]

33. Burdine, N.T. Relative Permeability Calculation from Pore Size Distribution Data. *Petr. Trans.Am. Inst. Min. Metall. Eng.* **1953**, *198*, 71–77. [CrossRef]

34. Di Prima, S.; Stewart, R.D.; Castellini, M.; Bagarello, V.; Abou Najm, M.R.; Pirastru, M.; Giadrossich, F.; Iovino, M.; Angulo-Jaramillo, R.; Lassabatere, L. Estimating the Macroscopic Capillary Length from Beerkan Infiltration Experiments and Its Impact on Saturated Soil Hydraulic Conductivity Predictions. *J. Hydrol.* **2020**, *589*, 125159. [CrossRef]

35. Haverkamp, R.; Ross, P.J.; Smettem, K.R.J.; Parlange, J.Y. Three-Dimensional Analysis of Infiltration from the Disc Infiltrometer: 2. Physically Based Infiltration Equation. *Water Resour. Res.* **1994**, *30*, 2931–2935. [CrossRef]

36. Angulo-Jaramillo, R.; Bagarello, V.; Di Prima, S.; Gosset, A.; Iovino, M.; Lassabatere, L. Beerkan Estimation of Soil Transfer Parameters (BEST) across Soils and Scales. *J. Hydrol.* **2019**, *576*, 239–261. [CrossRef]

37. Angulo-Jaramillo, R.; Bagarello, V.; Iovino, M.; Lassabatère, L. *Infiltration Measurements for Soil Hydraulic Characterization*; Springer International Publishing: Cham, Switzerland, 2016; ISBN 978-3-319-31786-1.

38. Philip, J.R. Stability Analysis of Infiltration. *Soil Sci. Soc. Am. J.* **1975**, *39*, 1042–1049. [CrossRef]

39. Zhang, R. Determination of Soil Sorptivity and Hydraulic Conductivity from the Disk Infiltrometer. *Soil Sci. Soc. Am. J.* **1997**, *61*, 1024. [CrossRef]

40. Gee, G.W.; Bauder, J.W. Particle-Size Analysis. In *SSSA Book Series*; Klute, A., Ed.; Methods of Soil Analysis, Part 1: Physical and Mineralogical Methods; Soil Science Society of America: Madison, WI, USA; American Society of Agronomy: Madison, WI, USA, 1986; pp. 383–411. ISBN 978-0-89118-864-3.

41. Kirkwood, T.B. *Geometric Means and Measures of Dispersion*; JSTOR: New York, NY, USA, 1979; ISBN 0006-341X.

42. Reynolds, W.D.; Drury, C.F.; Tan, C.S.; Fox, C.A.; Yang, X.M. Use of Indicators and Pore Volume-Function Characteristics to Quantify Soil Physical Quality. *Geoderma* **2009**, *152*, 252–263. [CrossRef]

43. Al-Nuaimy, W.; Huang, Y.; Shihab, S.; Eriksen, A. Automatic Target Detection in GPR Data. In Proceedings of the Ninth International Conference on Ground Penetrating Radar, Santa Barbara, CA, USA, 12 April 2002; Proc. SPIE 4758. Available online: https://www.spiedigitallibrary.org/conference-proceedings-of-spie/4758/1/Automatic-target-detection-in-GPR-data/10.1117/12.462232.short (accessed on 8 October 2024).

44. Holden, J. Hydrological Connectivity of Soil Pipes Determined by Ground-Penetrating Radar Tracer Detection. *Earth Surf. Process. Landf.* **2004**, *29*, 437–442. [CrossRef]

45. Birken, R.; Versteeg, R. Use of Four-Dimensional Ground Penetrating Radar and Advanced Visualization Methods to Determine Subsurface Fluid Migration. *J. Appl. Geophys.* **2000**, *43*, 215–226. [CrossRef]

46. RockWare Inc. RockWorks17 User's Manual. Available online: https://www.rockware.com/downloads/documentation/rockworks/rockworks17.pdf (accessed on 8 August 2019).

47. Attwa, M.; El-Shinawi, A. An Integrative Approach for Preliminary Environmental Engineering Investigations amidst Reclaiming Desert-Land: A Case Study at East Nile Delta, Egypt. *Environ. Earth Sci.* **2017**, *76*, 304. [CrossRef]

48. Lange-Athinodorou, E.; El-Raouf, A.A.; Ullmann, T.; Trappe, J.; Meister, J.; Baumhauer, R. The Sacred Canals of the Temple of Bastet at Bubastis (Egypt): New Findings from Geomorphological Investigations and Electrical Resistivity Tomography (ERT). *J. Archaeol. Sci. Rep.* **2019**, *26*, 101910. [CrossRef]

49. Longo, V.; Testone, V.; Oggiano, G.; Testa, A. Prospecting for Clay Minerals within Volcanic Successions: Application of Electrical Resistivity Tomography to Characterise Bentonite Deposits in Northern Sardinia (Italy). *J. Appl. Geophys.* **2014**, *111*, 21–32. [CrossRef]

50. Timlin, D.J.; Ahuja, L.R.; Ankeny, M.D. Comparison of Three Field Methods to Characterize Apparent Macropore Conductivity. *Soil Sci. Soc. Am. J.* **1994**, *58*, 278–284. [CrossRef]

51. Lassabatere, L.; Angulo-Jaramillo, R.; Goutaland, D.; Letellier, L.; Gaudet, J.P.; Winiarski, T.; Delolme, C. Effect of the Settlement of Sediments on Water Infiltration in Two Urban Infiltration Basins. *Geoderma* **2010**, *156*, 316–325. [CrossRef]

52. Smiles, D.; Knight, J. A Note on the Use of the Philip Infiltration Equation. *Soil Res.* **1976**, *14*, 103–108. [CrossRef]

53. Buczko, U.; Benz, O.; Hangen, E.; Brunotte, J.; Huttl, R. Infiltration and Macroporosity of a Silt Loam Soil under Two Contrasting Tillage Systems. *Landbauforsch. Volkenrode* **2003**, *53*, 181–190.

54. Stewart, R.D.; Bhaskar, A.S.; Parolari, A.J.; Herrmann, D.L.; Jian, J.; Schifman, L.A.; Shuster, W.D. An Analytical Approach to Ascertain Saturation-excess versus Infiltration-excess Overland Flow in Urban and Reference Landscapes. *Hydrol. Process.* **2019**, *33*, 3349–3363. [CrossRef]

55. Assouline, S.; Mualem, Y. Runoff from Heterogeneous Small Bare Catchments during Soil Surface Sealing. *Water Resour. Res.* **2006**, *42*, W12405. [CrossRef]

56. Mualem, Y.; Assouline, S.; Rohdenburg, H. Rainfall Induced Soil Seal (B) Application of a New Model to Saturated Soils. *CATENA* **1990**, *17*, 205–218. [CrossRef]

57. Assouline, S. Rainfall-Induced Soil Surface Sealing: A Critical Review of Observations, Conceptual Models, and Solutions. *Vadose Zone J.* **2004**, *3*, 570–591. [CrossRef]

58. Giunta, F.; Motzo, R.; Deidda, M. SPAD Readings and Associated Leaf Traits in Durum Wheat, Barley and Triticale Cultivars. *Euphytica* **2002**, *125*, 197–205. [CrossRef]

59. Kaye, J.P.; Quemada, M. Using Cover Crops to Mitigate and Adapt to Climate Change. A Review. *Agron. Sustain. Dev.* **2017**, *37*, 4. [CrossRef]

60. Lee, S.; McCann, L. Adoption of Cover Crops by U.S. Soybean Producers. *J. Agric. Appl. Econ.* **2019**, *51*, 527–544. [CrossRef]

61. Keesstra, S.; Rodrigo-Comino, J.; Novara, A.; Giménez-Morera, A.; Pulido, M.; Di Prima, S.; Cerdà, A. Straw Mulch as a Sustainable Solution to Decrease Runoff and Erosion in Glyphosate-Treated Clementine Plantations in Eastern Spain. An Assessment Using Rainfall Simulation Experiments. *CATENA* **2019**, *174*, 95–103. [CrossRef]